On the kinematics and dynamics parameters governing the flow in oscillating foils

On the kinematics and dynamics parameters governing the flow in oscillating foils

A. Cimarelli[a,*], M. Franciolini[b], A. Crivellini[c]

[a] *DIEF, University of Modena and Reggio Emilia, 41125 Modena, Italy*
[b] *USRA Fellow, NASA Ames Research Center, 94035 Mountain View CA, United States*
[c] *DIISM, Università Politecnica delle Marche, 60131 Ancona, Italy*

Abstract

Based on a high-order implicit discontinuous Galerkin method, numerical simulations of a two-dimensional oscillating foil are performed to explore the origin of basic aspects of the flow such as the generation of interesting flow structures in the wake and the associated aerodynamic forces. Dimensional arguments suggest that the flow is characterized by non dimensional aerodynamic coefficients depending on the kinematics of the oscillation, such its frequency and amplitude, and on the dynamics of the flow, such as the Reynolds number. Most of the studies have concentrated their attention on the role played by the kinematic of the oscillation with less or no attention to the effect of the Reynolds number. Here, we show that this effect cannot be neglected in the study of the phenomena at the basis of the generation of lift and thrust. We found that the Reynolds number plays a fundamental role for the development of thrust by defining critical values Re_c for the switch from drag to thrust conditions. It is also shown that for $Re > Re_c$, the Reynolds number defines additional subcritical values which are at the basis of flow instabilities leading to smooth and sharp transitions of the structure of the wake and of the related aerodynamic forces. For the analysis of the behaviour of the flow, the space of phases composed by the instantaneous lift and thrust (c_L, c_T) is introduced. It is shown how the orbits in the (c_L, c_T)-space allow us for a clear understanding of the physical evolution of the flow system and of the cyclical phenomena composing it.

Keywords: Oscillating foils, Reynolds number dependence of thrust, Deflected wake

1. Introduction

The unsteady fluid mechanics developed by oscillating foils is known to generate both thrust and lift. The understanding of the basic phenomena responsible for the generation of these aerodynamic forces triggered the interest of many researchers since long time. In particular, the ability of a flapping wing to create propulsion has been observed for the first time at the beginning of the last century by Knoller (1909) and Betz (1912) (the so-called Knoller-Betz effect). On the other hand, the first explanation of the generation of drag or thrust was given by von Kármán (1935) in terms of momentum deficit/excess behind the foil due to the location and orientation of the wake vortices. For a slowly oscillating foil, the structure of the wake is similar to the von Kármán vortex street observed behind bluff bodies and is found to induce a momentum deficit in the wake and, hence, drag. On the other hand, for a rapidly oscillating foil, the structure of the wake is inverted thus leading to a momentum excess behind the foil and, hence, thrust. It is however worth noting that, strictly speaking, the presence of an inverted von Kármán vortex street is a necessary but not sufficient condition for a momentum excess in the wake and, hence, to obtain a propulsive regime (Godoy-Diana et al., 2008, 2009; Das et al., 2016). Overall, the structure of the wake is recognized to be of overwhelming importance for the aerodynamic performance of oscillating foils. In this respect, it

*Corresponding author
Email address: andrea.cimarelli@unimore.it (A. Cimarelli)

is important to highlight that, for rapidly oscillating foils, symmetry breaking phenomena appear, leading to the formation of deflected wakes. As shown in Godoy-Diana et al. (2008) and Zheng and Wei (2012), the basic idea is that of a competing role played by the advection velocity of the vortex street and the self-advection of counter-rotating vortices in the near wake. The resulting effective velocity rules the trends of symmetry breaking and symmetry holding. The deflection angle of the wake can change from the near wake to the far wake regions as shown in Wei and Zheng (2014) where a model based on the Biot-Savart law is employed to demonstrate that this variation is induced by a changing of the orientation of the dipole structures of the wake and of their separation.

In accordance with these observations, the velocity of the oscillation has been recognized to represent the leading parameter governing the aerodynamic performances of the oscillating foil. The Garrick's linear theory confirms this expectation (Garrick, 1936). Indeed, by using the inviscid flat-plate theory of Theodorsen (1935), Garrick (1936) derived exact solutions where the production of thrust is shown to increase with the square of the non-dimensional flapping velocity. The importance of the velocity of the oscillation has been later verified in several works, see e.g. Triantafyllou et al. (1991); Lai and Platzer (1999); Floryan et al. (2017) and references therein. However, from dimensional arguments it is possible to show that the aerodynamic performances of such a flow system cannot be entirely described by using solely the non-dimensional velocity of the oscillation. Indeed, for a fixed flapping velocity, the physical problem can be characterized from a kinematic point of view also by different oscillation amplitudes and from a dynamic point of view by different ratios between inertial and viscous forces, the Reynolds number. However, a clear assessment of the role played by the Reynolds number is still lacking. This is due to the fact that most of the studies have been devoted to the understanding of the flow phenomena of a flapping foil as a function of the flapping velocity and amplitude, see e.g. Jones et al. (1998); Lewin and Haj-Hariri (2003); Andersen et al. (2017); Floryan et al. (2017). In particular, Jones et al. (1998) studied the appearance of deflected wake patterns where both an average thrust and an average lift are produced as a function of the kinematic parameters of the oscillation. They also suggest that this structure is a result of primarily inviscid phenomena. The changes of the wake pattern as function of the kinematic parameters of the oscillation have been further studied in Lewin and Haj-Hariri (2003), where the leading-edge vortex is found to play a primary role on the wake pattern depending on whether or not it is shed and on how it interacts with the trailing-edge vortex. The fate of the leading-edge vortex and its positive or negative reinforcement of the trailing-edge vortex is also correlated with the enhancement or reduction of thrust and of the propulsion efficiency. All these phenomena have been later rationalized using scaling laws in Floryan et al. (2017).

As already pointed out, only few works rigorously considered the effect of the Reynolds number even if this dependence is found to be not negligible, see e.g. Visbal (2009); Zheng and Wei (2012); Das et al. (2016); Senturk and Smits (2019). In fact, the wake deflection angle is found in Zheng and Wei (2012) to increase with the Reynolds number. Also the thrust performances are found to significantly increase with the Reynolds number in Das et al. (2016) and Senturk and Smits (2019). On the other hand, the thrust efficiency is found to reach a maximum for well-defined values of Reynolds number, which in turn depend on the kinematic parameters of the oscillation (Das et al., 2016; Senturk and Smits, 2019). In contrast with these results, it is worth mentioning the work of Van Buren et al. (2018) where a substantial independence of the thrust and power performances on the value of the free-stream velocity is claimed. Of particular relevance for the study of the Reynolds number effects is the work of (Das et al., 2016) where the aerodynamic performances of a NACA 0012 foil pitching about its quarter chord for a wide range of Reynolds numbers ($10 < Re < 2000$) is performed by using a high-resolution viscous vortex particle method. In addition to the above mentioned dependency of the propulsion efficiency on the Reynolds number and increase of thrust with the Reynolds number, it is also found that the von Kármán to reverse von Kármán wake transition precedes the drag-to-thrust transition independently on the Reynolds number. Further, the velocity of the oscillation values at which this transition occurs, are found to follow a power law scaling with the Reynolds number, $kh \sim Re^{-0.37}$, where kh is the heave velocity ratio defined in section 2. Finally, the peak of propulsive efficiency is found to occur for oscillating velocity values that exceed those for the onset of the wake deflection, so that the peak propulsive efficiency was always achieved in the deflected wake regime.

In the present work, we aim at systematically addressing these issues by studying the role of the Reynolds

number as a function of the kinematic parameters of the oscillation. The basic aspects of the flow such as the structure of the wake and the associated aerodynamic forces will be assessed. To this end, high-order accurate numerical simulations based on a discontinuous Galerkin method of a rigid foil in a two-dimensional free stream with prescribed heaving motions will be studied by systematically varying the Reynolds number for fixed couples of heave velocity and amplitude. The range of Reynolds numbers covered is $50 \leq Re \leq 5000$, which allows us to assess the flow properties in the laminar two-dimensional regime. Indeed, the high Reynolds number behaviour of oscillating foils is characterized by three-dimensional phenomena due to the laminar to turbulent transition of the flow. In this regime, the Reynolds number still plays a role for the aerodynamic performances of the system as shown in Isogai et al. (1999); Ashraf et al. (2011); Dave et al. (2020) where Reynolds Average Navier-Stokes (RANS) simulations have been used. Here, we limit our analysis to the instabilities and aerodynamic performances of oscillating foils in the laminar two-dimensional regime.

The paper is organized as follows. In section 2, the dimensionless groups used to analyse the flow are introduced while in section 3 the numerical details of the simulations performed are reported. The aerodynamic performances and the structure of the wake as a function of the dimensionless parameters governing the flow are analysed in sections 4 and 5, respectively. The role of the Reynolds number is carefully addressed in section 6 and its relation with the behaviour of the leading-edge vortex shedding is analysed in section 7. The paper is finally closed by final remarks in section 8 and by Appendix A where it is shown how results change by dealing with other type of dimensionless groups.

2. Dimensionless groups

We consider the flow around a two-dimensional rigid foil of chord c oscillating in the vertical direction. The free-stream velocity is a flat unperturbed profile U_∞ and the vertical oscillation of the foil follows an harmonic law,

$$y(t) = h\ sin(2\pi f t)\ , \tag{1}$$

where h is the vertical displacement, f is the frequency and t the time. In the present work, (x, y) denote the streamwise and vertical coordinates and the corresponding velocities are (u, v). In terms of velocity, the vertical oscillation reads,

$$v(t) = 2\pi f h\ cos(2\pi f t) = V cos(2\pi f t)\ . \tag{2}$$

where $V = 2\pi f h$ is the maximum vertical velocity associated with the oscillation. Classical dimensional analysis techniques lead to the following dimensionless groups for the study of the aerodynamic forces,

$$C_D = \frac{D}{1/2\rho s c U_\infty^2} = f\left(\frac{fc}{U_\infty}, \frac{h}{c}, \frac{U_\infty c}{\nu}\right) \qquad C_L = \frac{L}{1/2\rho s c U_\infty^2} = g\left(\frac{fc}{U_\infty}, \frac{h}{c}, \frac{U_\infty c}{\nu}\right) \tag{3}$$

where D and L are the average drag and lift forces, ρ is the density of the fluid, ν is the kinematic viscosity and s is the span of the foil. In the dimensionless parameters governing the flow,

$$St = \frac{fc}{U_\infty}\ ; \qquad KC = \frac{h}{c}\ ; \qquad Re = \frac{U_\infty c}{\nu}\ ; \tag{4}$$

we can recognized the chord-based Strouhal number of the oscillation St, the amplitude of the oscillation KC also known as Keulegan-Carpenter number and the Reynolds number Re. The product of St with KC is the so-called amplitude-based Strouhal number,

$$kh = 2\pi\ KC\ St = \frac{V}{U_\infty} \tag{5}$$

which represents the ratio between the heave velocity V and the free-stream speed U_∞ and it is found to play a central role in describing the transition from drag to thrust (Triantafyllou et al., 1991; Lai and Platzer, 1999; Floryan et al., 2017). For this reason, in the present work we will consider the behaviour of the flow as

a function of the heave velocity ratio kh rather than of the chord-based Strouhal number St. By considering the power consumption related to the imposed vertical oscillation, $P_{in} = F_y v$ with F_y the instantaneous vertical aerodynamic force, and the net power eventually associated with thrust, $P_{out} = F_x U_\infty$ with F_x the instantaneous streamwise aerodynamic force, it is possible to define a parameter quantifying the average efficiency of the oscillation as

$$\eta = \frac{\int P_{out} dt}{\int P_{in} dt} \ , \tag{6}$$

that in terms of aerodynamic coefficients can be written as $\eta = C_D/C_P$ where C_P is the power coefficient.

It is worth mentioning, that the drag and lift coefficients and the relative governing parameters introduced in (3) represent classical non-dimensional groups commonly used in non-oscillating foils. However, other dimensionless groups can be defined. As an example, based on dimensional parameters solely related with the kinematics and dynamics of the oscillation, different governing parameters and aerodynamic coefficients can be obtained with some interesting properties as shown in Appendix A.

3. Numerical technique and simulations

3.1. Solver

The numerical simulations were performed using a high-order implicit discontinuous Galerkin (DG) method, see Bassi et al. (2005, 2007); Crivellini et al. (2013a,b). The advantage of using such methods is related to the ability of providing very accurate solutions on stretched, curved and possibly hybrid computational grids. In this work, we consider a two-dimensional incompressible DG code, suitably extended to deal with a non-inertial reference frame to account for the foil oscillations. The system of equation is expressed as a function of the absolute velocity u_i observed from a moving reference frame of velocity components U_j, such that

$$\begin{aligned} \partial_i u_i &= 0 \\ \partial_t u_i + \partial_j (u_j u_i) &= -\partial_i p/\rho + 1/Re\, \partial_j^2 u_i + U_j \partial_j u_i \ , \end{aligned} \tag{7}$$

where $Re = U_\infty c/\nu$ is the Reynolds number. Note that c and U_∞ are hereafter used as reference length and velocity scales. The DG discretization can be obtained by expressing the system (7) in variational form, decomposing the domain by elements, and defining an appropriate polynomial space of order p within each element. In this work the convective numerical fluxes that are used to couple the solution at the interior faces of the mesh, are computed through the artificial compressibility flux method of Bassi et al. (2006). On the other hand, the second form of the Bassi and Rebay scheme, see Bassi et al. (2005), has been used for the viscous terms. Boundary conditions are applied in weak form by properly defining an external state to compute the numerical fluxes at boundaries. The implicit time discretization is obtained through the use of a three-stage, order-three linearly-implicit Rosenbrock-type Runge–Kutta scheme named ROS3P by Lang and Verwer (2001). The linear systems arising from this discertization were handled using a flexible GMRES solver preconditioned by a p-multigrid algorithm described by Franciolini et al. (2020). This solution procedure is parallel efficient, which has been relevant for the work.

To validate the solver, we consider the flow around a transversely oscillating cylinder. This test case has been chosen because of the availability of reference data at well-specified values of the three governing parameters (KC, kh, Re) reported in Guilmineau and Queutey (2002). This flow has been solved at $Re = 185$, $KC = h/d = 0.2$ and at six frequencies $f = kf_0$, where d is the cylinder diameter and f_0 is the natural vortex-shedding frequency (corresponding to a Strouhal number $St = f_0 D/U_\infty = 0.195$). The computational domain is a square with the side equal to $100d$, while the grid consists of 1809 rectangular elements with a third order piecewise polynomial representation of the faces at the cylinder wall. As for the foil simulations reported in the present work, the sixth order polynomial approximation of the solution and the ROS3P Rosenbrock scheme were adopted. The Δt was 10^{-1} for all the case, which means at least 42 time steps for each oscillation period. Figure 1(a) reports the computed force coefficients and the references values from Guilmineau and Queutey (2002). The agreement is very good including the frequency at which

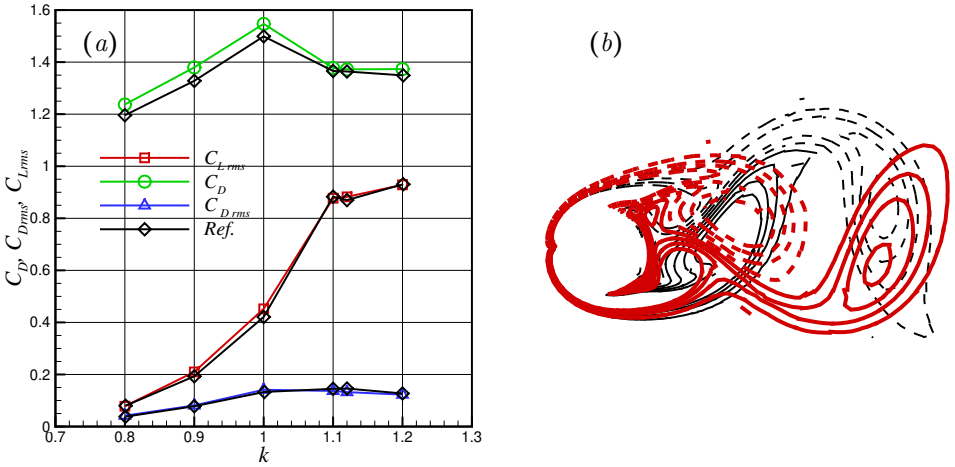

Figure 1: Transversely oscillating cylinder at $Re = 185$, $KC = h/d = 0.2$. (a) Comparison of the force coefficients with the reference values digitalized from Guilmineau and Queutey (2002). (b) Iso-lines of vorticity for $k = 1$, thin lines in black, and for $k = 1.12$, thick lines in red, at the lower vertical position; solid lines for positive values, dashed lines for negative values.

the so called vortex switching occurs, *i.e.* at $k = 1.1$, which is also very close to the experimental value reported in Gu et al. (1994) at $k = 1.12$. As reported in those references, this phenomenon is characterized by the switch of the vortical structures location with respect to the cylinder side at the extreme vertical positions of the oscillation, as shown in figure 1(b) for the $k = 1$ and $k = 1.12$ cases.

3.2. Simulation settings

The study of the aerodynamic performances of oscillating foils is here performed by considering a NACA 0012 foil at zero incidence. The set of equations is solved by using a sixth order polynomial representation of the solution, $p = 6$, which means that the velocity components are 7^{th} order accurate and pressure 6^{th} order accurate. The unperturbed velocity field U_∞ is used as initial condition. A circular computational domain centred at the leading-edge of the foil is employed of radius $r = 25$. Considering the nature of the equation set, the wall boundary is prescribed by imposing U_i, while at the outer boundary the free stream state (p_∞,U_∞) is imposed. The boundary layer region is discretized using structured-like quadrangular elements suitably curved to accurately represent the foil curvature. To this end, a piecewise third-order polynomial approximation of the faces of the elements is employed. The baseline grid is composed by 7416 elements that, by considering a $p = 6$ approximation, leads to solutions with a number of degrees of freedom 207648. The time step size, Δt, has been chosen according to the frequency of the oscillation f. For example, most of the computations were performed with $1/(f\Delta t) \simeq 80$ to ensure the results to be independent of the time discretization.

Although each simulation involves a number of DOFs not particularly large, a long time integration, typically of the order of $O(1000/f)$ was found to be necessary to perform well-converged statistics and to observe the slow inversion of the deflected wake as described in sections 5 and 6. Statistics are indeed computed by performing a time average. Due to the periodicity of the flow problem, this procedure is applied to a time window whose width is an integer number of the foil oscillating period. Statistics are computed by discarding the flow transition from the initial conditions (typically of the order of $O(50/f)$), using a number of oscillating periods of the order of $O(200/f)$ for the flow cases with a stationary wake and of $O(1000/f)$ for the flow cases showing a very slow unsteadiness of the wake.

To prove the accuracy of the results, we have performed a study of the numerical convergence of the solutions by varying the grid resolution and the domain size. Here, we report the representative case at $Re = 1500$, $KC = 0.12$ and $kh = 0.9$. Figures 2(a) and (b) report the instantaneous iso-lines of vorticity obtained by a couple of simulations. In figure 2(a), the result of our baseline numerical settings,

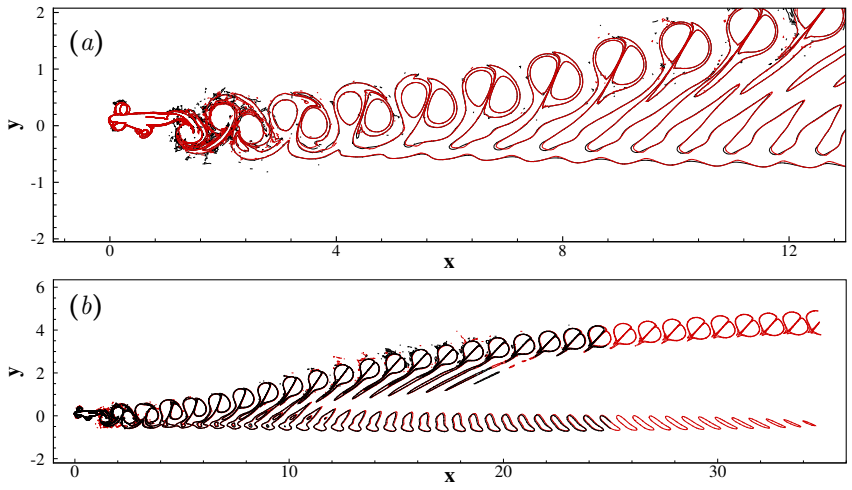

Figure 2: (a) Comparison of the instantaneous vorticity pattern, $\omega_z = [-0.25, 0.25]$, obtained with a fine and coarse mesh denoted respectively with black and red contour lines. (b) Comparison of the instantaneous vorticity pattern, $\omega_z = [-0.25, 0.25]$, obtained from two different numerical domain extents denoted respectively with black and red contour lines.

a grid consisting of 7416 elements solved using a $p = 6$ approximation (207648 DOFs for each equation), is superimposed to that obtained with 23808 elements and $p = 5$ (499968 DOFs). The agreement in terms of instantaneous and local behaviours is clearly very good; a similar result is obtained using different time step sizes, *i.e.* $\Delta t = 1/(80f)$ or $1/(160f)$. From a global point of view, the maximum difference of the aerodynamic performances C_T, C_L and η measured from the finer and coarser simulations is of the order of 0.3%.

In figure 2(b), the sensitivity of the results to the domain size is shown. Note that, since the wake at this regime is strongly inclined, this test is particularly relevant. The grid density and the polynomial approximation ($p = 6$) are the same in both the cases, but since in one case the domain is significantly larger than the other, the outer boundary is a circumference of radius $35c$ against $25c$, the number of employed elements raises from the baseline value 7416 to 12034. The perfect agreement of the local and instantaneous behaviours, even in correspondence of the outer boundary, justified the use of the smaller domain for all the the cases reported herein. Also from a global point of view, the maximum difference of the aerodynamic performances C_T, C_L and η measured from the larger and smaller simulation domains is of the order of 0.1%.

4. Aerodynamic performances

In this section we briefly highlight the effect of each of the three governing parameters (KC, kh, Re) on the aerodynamic performances of the flow around an oscillating NACA 0012 foil at zero incidence. The list of the simulated governing parameters and of the relative aerodynamic performance is reported in table 1.

Let us start with the analysis of the behaviour of thrust, $C_T = -C_D$. In figure 3(a), the behaviour of thrust as a function of the heave velocity ratio kh is shown for different couples of Reynolds numbers Re and amplitude ratios KC. In accordance with several literature results, thrust appears to increase with kh, see e.g. Garrick (1936); Triantafyllou et al. (1991); Lai and Platzer (1999); Floryan et al. (2017). In particular, for small values of the heave velocity ratio, such as for $kh = 0.3$, the oscillating foil experiences drag, $C_T < 0$, while for higher values of kh thrust is produced, $C_T > 0$. In this respect, let us point out that other possible dimensionless groups based on pure kinematic and dynamic properties of the flow oscillation could unveil the origin of such a scaling of thrust as shown in Appendix A.

As shown by the different curves in figure 3(a), the behaviour of thrust is however affected also by the values of the other two governing parameters KC and Re. As far as it concerns the effect of the heave

Case	KC	kh	Re	C_T	C_L	η	Case	KC	kh	Re	C_T	C_L	η
L1	0.12	0.3	500	-0.139	null	-1.352	L6	0.24	0.3	500	-0.119	null	-0.866
H1	0.12	0.3	1500	-0.051	null	-0.464	H6	0.24	0.3	1500	-0.040	null	-0.273
L2	0.12	0.6	500	-0.018	null	-0.029	L7	0.24	0.6	500	-0.020	null	-0.866
H2	0.12	0.6	1500	0.087	null	0.132	H7	0.24	0.6	1500	0.077	null	-0.273
L3	0.12	0.9	500	0.250	null	0.117	L8	0.24	0.9	500	0.199	null	0.114
H3	0.12	0.9	1500	0.325	0.279	0.150	H8	0.24	0.9	1500	0.260	null	0.143
L4	0.12	1.2	500	0.680	0.175	0.123	L9	0.24	1.2	500	0.470	null	0.113
H4	0.12	1.2	1500	0.801	null	0.144	H9	0.24	1.2	1500	0.483	null	0.115
L5	0.12	1.5	500	1.265	-4.475	0.113	L10	0.24	1.5	500	1.165	null	0.120
H5	0.12	1.5	1500	1.176	null	0.104	H10	0.24	1.5	1500	0.983	null	0.104

Table 1: Parameters, aerodynamic coefficients and efficiency of the simulated flow cases.

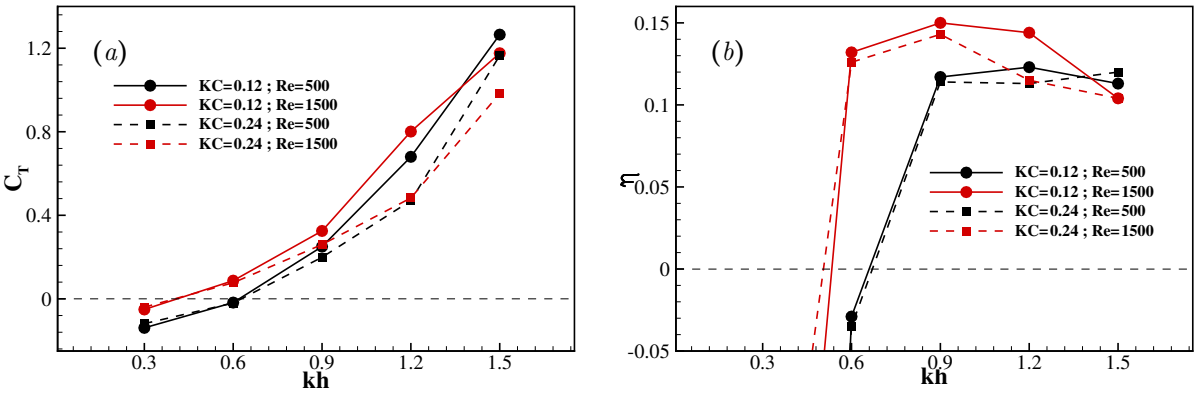

Figure 3: Thrust (a) and efficiency (b) as a function of the heave velocity ratio kh and for different couples of Reynolds number Re and heave amplitude KC.

amplitude KC, by comparing the curves denoted by circles with those denoted by squares with the same colour (same Reynolds number Re), it is possible to see a double effect of KC. In particular, when drag is produced such as for small heave velocity ratio, $kh = 0.3$, increasing the heave amplitude leads to a slight decrease of drag. On the other hand, when thrust is produced for higher velocity ratios, the effect of KC is to decrease thrust. These effects, despite not negligible, are less intense than those of the heave velocity ratio and hence, do not shade the increasing of thrust with kh at least for the two values $KC = 0.12$ and $KC = 0.24$ considered.

A double effect is observed also for the Reynolds number which depends on the value of the heave velocity ratio, kh. In particular, for relatively small values, $kh \leq 1.2$, the effect of Re is to decrease drag and to increase thrust in accordance with results from Das et al. (2016). On the contrary, for higher values, $kh = 1.5$, the effect of Re is to decrease thrust.

We analyse now the efficiency of the oscillation to obtain thrust, η, as a function of the governing parameters (KC, kh, Re). Before that, let us notice that due to its definition (6), η is characterized by negative values when the oscillating foil experiences drag while, on the other hand, is positive when thrust is generated. Hence, η ranges from $-\infty$ for a drag in a non-oscillating foil to 1 in the ideal case of a power thrust equals to the power consumption of the oscillation. We start the analysis by considering the behaviour of η as a function of the heave velocity ratio kh and for different couples of Reynolds numbers Re and amplitude ratios KC shown in figure 3(b). For small kh the oscillating foil experiences drag so that negative values of η are measured. On the other hand, for higher heave velocity ratios positive efficiencies are measured due to the generation of thrust. In particular, the efficiency of the oscillation increases with

the heave velocity eventually approaching a maximum. The intensity of this maximum and the position in the space of the heave velocity amplitude kh significantly depends on the value of the other two governing parameters particularly of the Reynolds number. In fact, a more intense peak of efficiency and a shift of its location towards smaller values of kh is observed by increasing the Reynolds number (Das et al., 2016). The effect of the heave amplitude KC is less significant for the efficiency of the oscillation being responsible for very small variations of η as far as only flow cases characterized by positive efficiencies are considered.

5. Flow topology

In this section, we analyse the effect of the governing parameters on the main flow features generated by the oscillating foil. To this aim we consider the pattern taken by the instantaneous vorticity $\omega_z = \partial v/\partial x - \partial u/\partial y$ in the (x, y)-space. This approach allows us to appreciate the structure of the wake which is known to play a fundamental role in the determination of the thrust properties (Das et al., 2016). Furthermore, the phenomenon of deflection of the wake, known to occur in such a flow for certain values of the governing parameters, can be easily observed. As it will be shown in the following, when the deflection of the wake is stationary, i.e. no upward/downward switching of the deflection occurs in time, this phenomenon can be associated with the generation of non-zero average lift, $C_L \neq 0$. The reader interested on the mechanisms at the basis of the symmetry breaking of the reverse von Kármán vortex street produced by a flapping foil and on their modelling is referred to Godoy-Diana et al. (2009); Zheng and Wei (2012); Wei and Zheng (2014) and references therein. Finally, to better understand the temporal evolution of the developed flow, we will make use of phase diagrams (c_L, c_T), where c_L and c_T are the instantaneous lift and thrust coefficients, and prove their suitability for the understanding of the main unsteadinesses of the flow (Bose and Sarkar, 2018).

5.1. Small heave velocity ratio, $kh = 0.3$

In figure 4, the instantaneous vorticity pattern and the phase diagrams of the simulated flow cases for small heave velocity ratio $kh = 0.3$ are shown. Let us recall that for this value of heave velocity, the oscillating foil experiences drag, $C_T < 0$, for all the combinations of the other parameters KC and Re considered.

As shown in figure 4(a), for the low heave amplitude and Reynolds number case, $KC = 0.12$ and $Re = 500$, a classical von Kármán street is observed. The phase diagram (c_L, c_T) shows the orbit followed by the lift and thrust coefficients during the oscillating period. The attractor is a periodic limit cycle which shows that the positive and negative fluctuations of lift during the oscillating periods are symmetric ($C_L = 0$) and that the fluctuations of thrust are always negative ($C_T < 0$). By increasing the Reynolds number and retaining the same value of heave amplitude, $Re = 1500$ and $KC = 0.12$, the pattern of the wake modifies, see figure 4(b). In particular, a slightly inverted von Kármán street is observed. Such a phenomenon is commonly related with the appearance of thrust. Indeed, as shown by the phase diagram (c_L, c_T), the orbit is shifted in the upward direction towards smaller values of drag. Consistently, we measure a reduction of drag with respect to the lower Reynolds number case, see flow cases L1 and H1 reported in table 1.

Almost the same observations can be done for the two cases at higher heave amplitude $KC = 0.24$ shown in figure 4(c) and (d). Indeed, we observe a reduction of drag by moving from the lower to the higher Reynolds number case consisting in a upward shift of the orbit of the limit cycle together with the appearance of phases of the oscillating period producing a net thrust. The main difference with respect to the lower heave amplitude case described so far concerns the topology of the wake. Indeed, by increasing the Reynolds number, the flow pattern of the wake significantly changes from a classical von Kármán street to a wake composed by the simultaneous shedding for each oscillating period of two vortex pairs and two single vortices (Williamson and Roshko, 1988).

5.2. Intermediate heave velocity ratio, $kh = 0.9$

In figure 5, the instantaneous vorticity pattern and the phase diagrams of the simulated flow cases for intermediate heave velocity ratio $kh = 0.9$ are shown. Let us recall that for this value of heave velocity, the

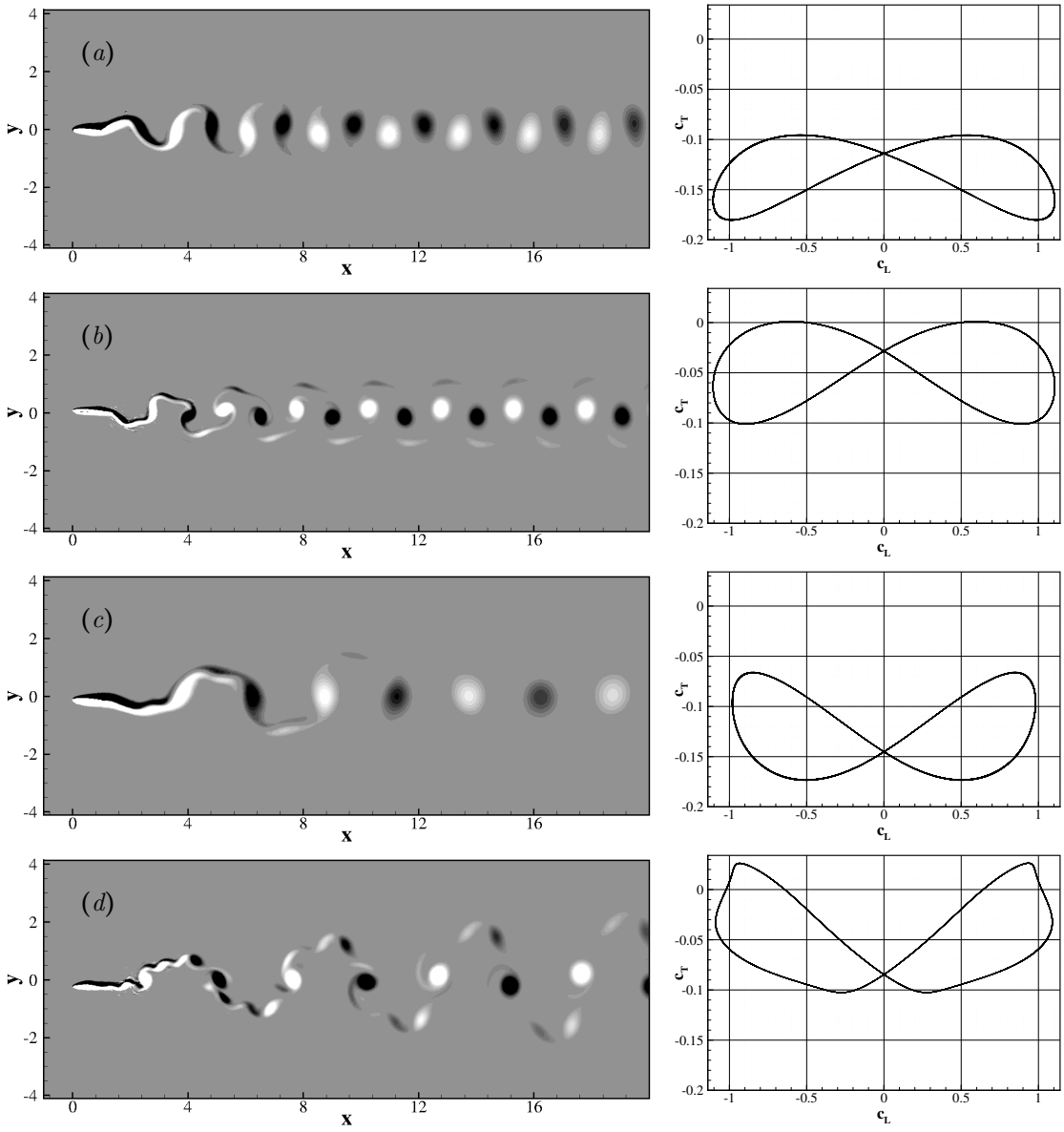

Figure 4: Vorticity contours for $kh = 0.3$ and phase diagrams (c_L, c_T). Flow cases L1 (a), H1 (b), L6 (c) and H6 (d). The range of values shown are $\omega_z = [-1, 1]$.

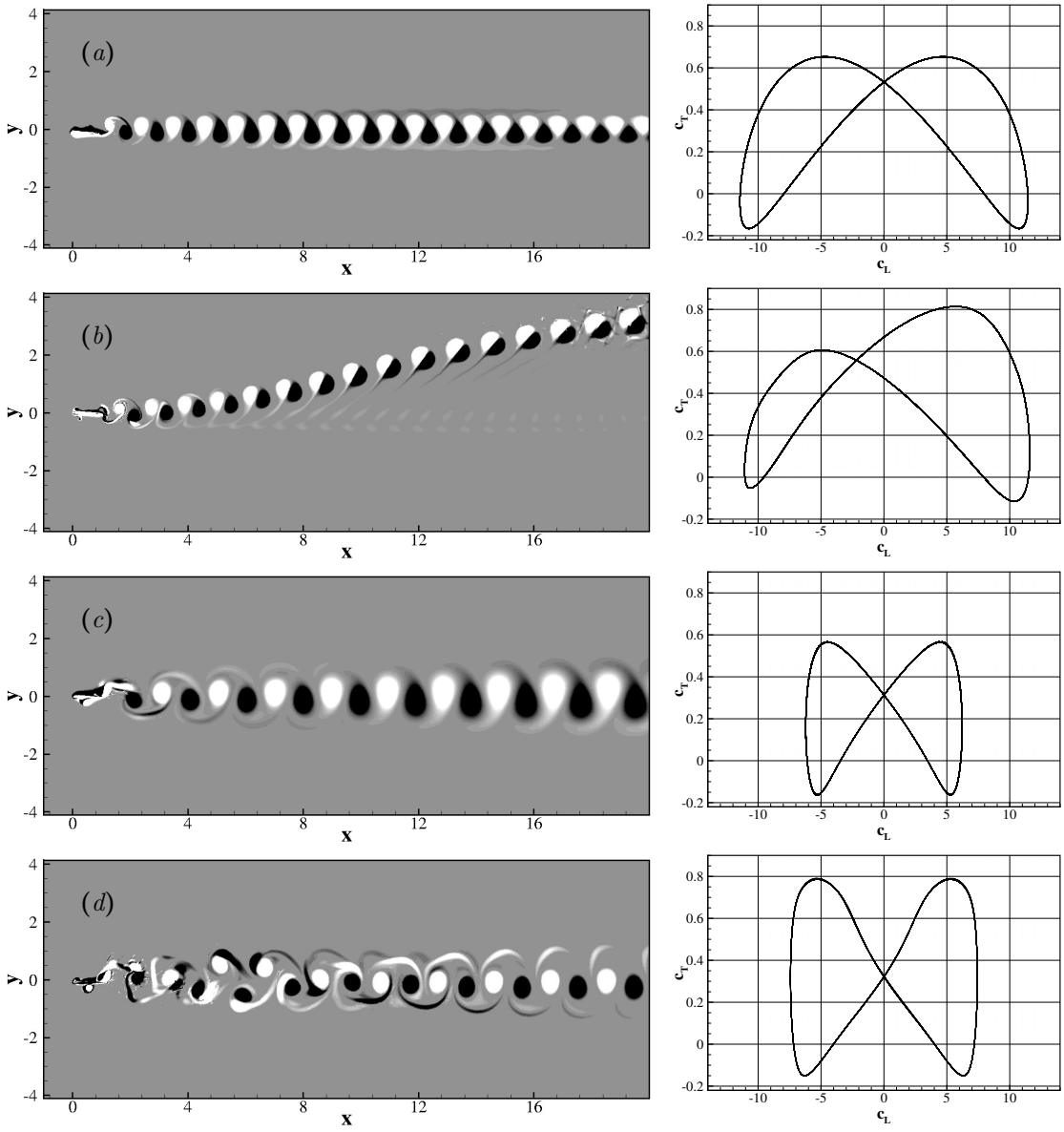

Figure 5: Vorticity contours for $kh = 0.9$ and phase diagrams (c_L, c_T). Flow cases L3 (a), H3 (b), L8 (c) and H8 (d). The range of values shown are $\omega_z = [-1, 1]$.

oscillating foil experiences thrust, $C_T > 0$, for all the combinations of the other parameters KC and Re considered.

As shown in figure 5(a), for the low heave amplitude and Reynolds number case, $KC = 0.12$ and $Re = 500$, an inverted von Kármán street is observed. The corresponding orbit in the phase diagram (c_L, c_T) is a limit cycle where the positive and negative fluctuations of lift are symmetric ($C_L = 0$) and thrust, $c_T > 0$, is experienced by the foil for almost the entire periodic cycle. By increasing the Reynolds number $Re = 1500$ and retaining the same heave amplitude $KC = 0.12$, an interesting phenomenon of stationary deflection of the wake is observed. As shown by the phase diagram, such a deflection of the wake results in a periodic orbit following a non-symmetric limit cycle. As shown in the previous section, another effect of the increase of the Reynolds number is also of a net increasing of thrust. By comparing the phase diagrams in figure 5(a) and (b), it is possible to see that such an increase of thrust is almost obtained during half a period of the asymmetric limit cycle.

For the same value of kh, such a deflection of the wake was not observed in Lewin and Haj-Hariri (2003) and Jones et al. (1998). Indeed, these works were conducted at a lower Reynolds number corresponding to our L3 case where, accordingly, we observe a straight wake. In the above mentioned works, a wake inflection was observed only for $kh = 1.5$ in conjunction with a periodic phenomenon of upward/downward switching of the direction of the deflection. In the present case at a lower frequency of the oscillation, $kh = 0.9$, and higher Reynolds number $Re = 1500$, such a periodic inversion of the wake is not observed as it will be on the contrary observed for $kh = 1.5$ as shown in the following section.

The same effect of the Reynolds number is not observed for higher heave amplitudes, $KC = 0.24$, shown in figures 5(c) and (d). In this case, the increasing of the Reynolds number from $Re = 500$ to $Re = 1500$ does not lead to the same phenomenon of deflection of the wake. Indeed, both the periodic orbits follow a symmetric limit cycle corresponding to a straight wake and zero lift $C_L = 0$. The only effect of the Reynolds number is a slight modification of the wake which leads to an increase of thrust as can be appreciated by the upward shift of the phase diagram.

5.3. High heave velocity ratio, $kh = 1.5$

In figure 6, the instantaneous vorticity pattern and the phase diagrams of the simulated flow cases for high heave velocity ratio $kh = 1.5$ are shown. Let us recall that for this value of heave velocity, the oscillating foil experiences the highest values of thrust measured in the present set of simulations. As it can be seen in figure 6, the common feature of the flow at high heave velocity is the less coherent pattern taken by the wake. In particular, for the small Reynolds number, $Re = 500$, shown in panels 6(a) and (c), a vortex pattern can be still recognized. On the contrary, for the higher Reynolds number, $Re = 1500$, shown in panels 6(b) and (d), a fully chaotic flow feature is observed in the wake. In the space of phases such phenomena result in phase orbits which not follow any more a limit cycle but are chaotically confined to follow a strange attractor.

Let us analyse in detail the behaviour of the flow for small Reynolds number and heave amplitude, $Re = 500$ and $KC = 0.12$, shown in figure 6(a). An unstable asymmetric wake can be recognized. However, as shown by the phase diagram, such a chaotic deflection of the wake appears to be locked in one side, i.e. no upward/downward switch in time of the deflection of the chaotic wake occurs. In particular, as shown by the red line, the orbits are such that every two oscillating periods almost the same paths are followed but no tendency towards an inversion of the asymmetry (deflection of the wake) appears. Analogously to the stationary deflected wake observed so far at intermediate heave velocity ratio (flow case H3), the present flow case at high heave velocity (L5) also leads to a non-zero average lift, see table 1. The main difference between the two cases is the chaotic feature of the high heave velocity regime, so that the deflection of the wake is stationary in a statistical sense.

By increasing the Reynolds number, $Re = 1500$ figure 6(b), the most evident effect is an increase of the complexity of the wake. However, as apparent from the phase diagram, the overall behaviour of the orbits is such that the region of phases covered is now symmetric and, hence, a statistically zero lift is measured contrary to the lower Reynolds number case, see table 1. A careful inspection of the phase diagram reveals that, actually, the flow is locked in a state of chaotically deflected wake for many periods of oscillation of

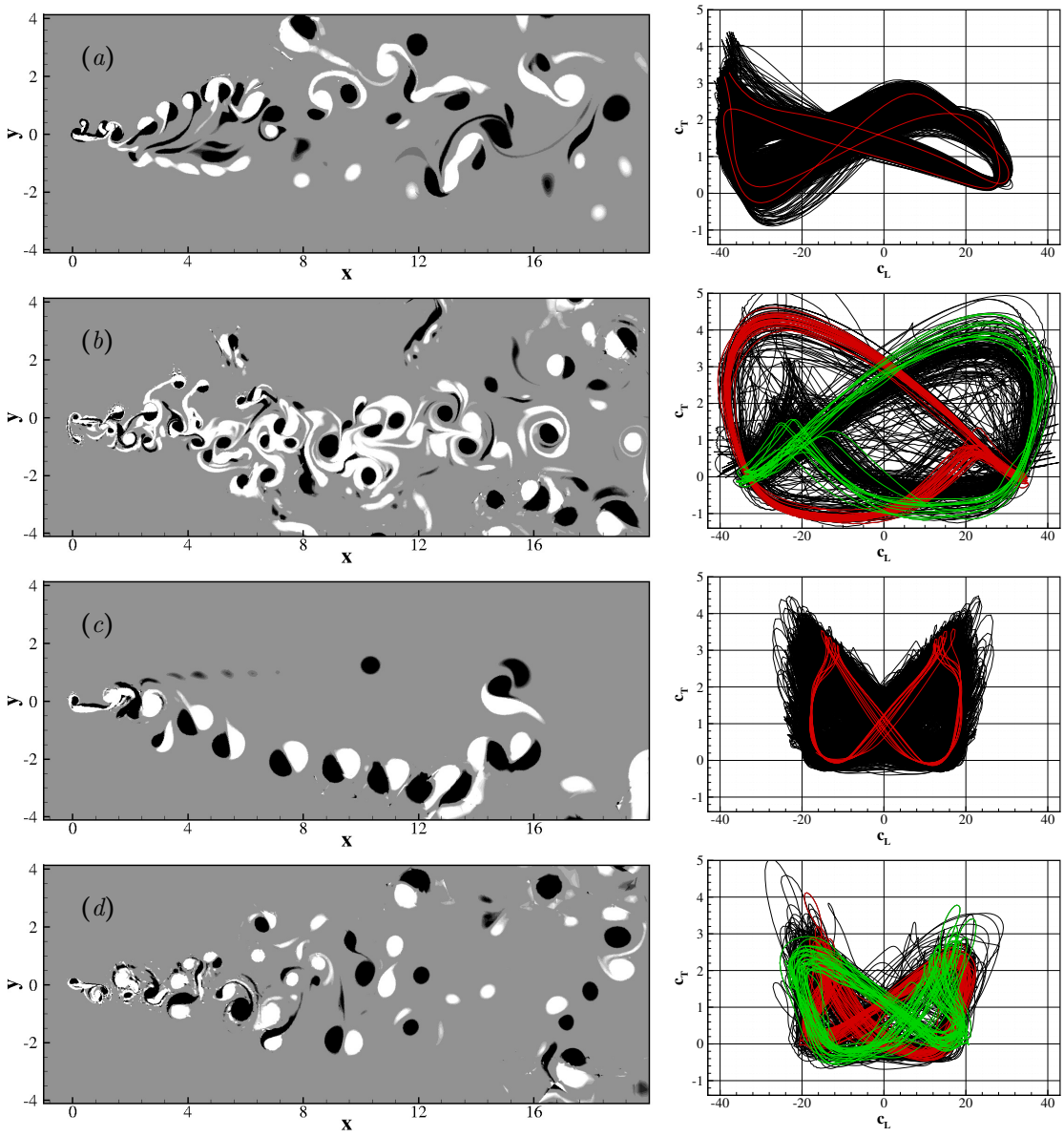

Figure 6: Vorticity contours for $kh = 1.5$ and phase diagrams (c_L, c_T). Flow cases L5 (a), H5 (b), L10 (c) and H10 (d). The range of values shown are $\omega_z = [-1, 1]$.

the order of $\mathcal{O}(100)$ (see Heathcote and Gursul (2007) where similar values are reported) as shown by the two opposite and strongly asymmetric paths followed by the orbits (green and red lines). Hence, the picture is that of orbits locked in significantly asymmetric paths (locked deflected wake) for long periods followed by a sharp inversion of the asymmetry (inversion of the deflection of the wake). Such a phenomenon of switching has been already observed in several works, see e.g. Jones et al. (1998); Lewin and Haj-Hariri (2003); Heathcote and Gursul (2007); Wei and Zheng (2014). However, let us remark that such a coherent time-dependent pattern behind the chaotic overall behaviour of the flow can be rigorously revealed only by using the phase diagrams. As already shown in figure 3, the effect of the Reynolds number for high heave velocity ratios is to decrease thrust. As shown in quantitative terms by the phase diagrams in panels 6(a) and (b), such a phenomenon is a result of downward shift of the attractor so that the foil for a significant part of the oscillating period experiences also drag.

Let us now study the effects of the heave amplitude KC. For low Reynolds numbers, $Re = 500$, the statistically asymmetric wake observed in panel 6(a) disappears by increasing the heave amplitude from $KC = 0.12$ to $KC = 0.24$, panels 6(a) and (c), leaving space to a statistically symmetric wake thus recovering a zero average lift, $C_L = 0$. As shown by the phase diagram in panel 6(c), the recovery of a symmetric wake and zero average lift is not achieved with a low frequency phenomena of inversion of a strongly asymmetric wake such as for the lower heave amplitude case at larger Reynolds number, $KC = 0.12$ and $Re = 1500$, panel 6(b). Indeed, as shown with a red line reporting the behaviour of seven oscillating periods, for each period of oscillation the orbit is weakly asymmetric so that the entire space of phases is covered by a smoothly varying asymmetric phenomenon. For the higher Reynolds number case, $Re = 1500$, the effect of the heave amplitude is less significant, compare panels 6(b) and (d). As shown by the phase diagrams, the flow experiences a low frequency unsteadiness of the order of $\mathcal{O}(100)$ oscillating periods so that in both cases, $KC = 0.12$ and $KC = 0.24$ for $Re = 1500$, strongly asymmetric orbits are performed for long periods (locked deflected wake) which are followed by a sharp switching of the asymmetry (inversion of the wake deflection).

6. On the effect of the Reynolds number

In the previous section we have shown how a careful inspection of the entire space of parameters governing the flow around an oscillating foil allows us to rigorously understand the net effect of each of them by keeping fixed the other two. In the present section, we restrict the field of investigation by solely addressing the role of the Reynolds number. In particular, we will analyse the effect of the Reynolds number for heave velocity and amplitude $(KC, kh) = (0.12, 0.9)$. Indeed, in the previous section 5, we found that, by varying the Reynolds number for these values of KC and kh, interesting flow phenomena appear such as the occurrence of steady deflected wakes. To this end we performed 41 additional simulations by varying the Reynolds number from $Re = 50$ to $Re = 5000$ keeping fixed the heave amplitude and velocity at $(KC, kh) = (0.12, 0.9)$, see table 2.

In accordance with the analysis of the aerodynamic performances reported in section 4, for $kh = 0.9$, the effect of the Reynolds number is to enhance both the thrust and the efficiency of the oscillation. As shown in the insets of figure 7(a) and (c), this increase is particularly evident by increasing the Reynolds number up to $Re = 850$. As shown in the main panels of figure 7, by further increasing the Reynolds number, $Re > 850$, the increase of C_T and η becomes piecewise continuous being alternated with discontinuous jumps corresponding to the appearance of interesting flow phenomena. For this reason, in what follows, we will analyse the main flow features by dividing the entire range of Reynolds numbers considered in five relevant subregions.

6.1. Region I

As shown in figure 7, by increasing the Reynolds number up to $Re = 725$ (region I), both thrust and efficiency are drastically enhanced, while, the lift coefficient is always zero. The strength of the effect of Re is such that for the lower Reynolds number cases, $Re < 200$, the oscillating foil experiences drag while for $Re \geq 200$, thrust conditions are recovered. Hence, in analogy with the heave velocity ratio kh that has been widely used to identify the critical conditions for the development of thrust, also the Reynolds number plays this role by defining critical values above which thrust conditions are developed.

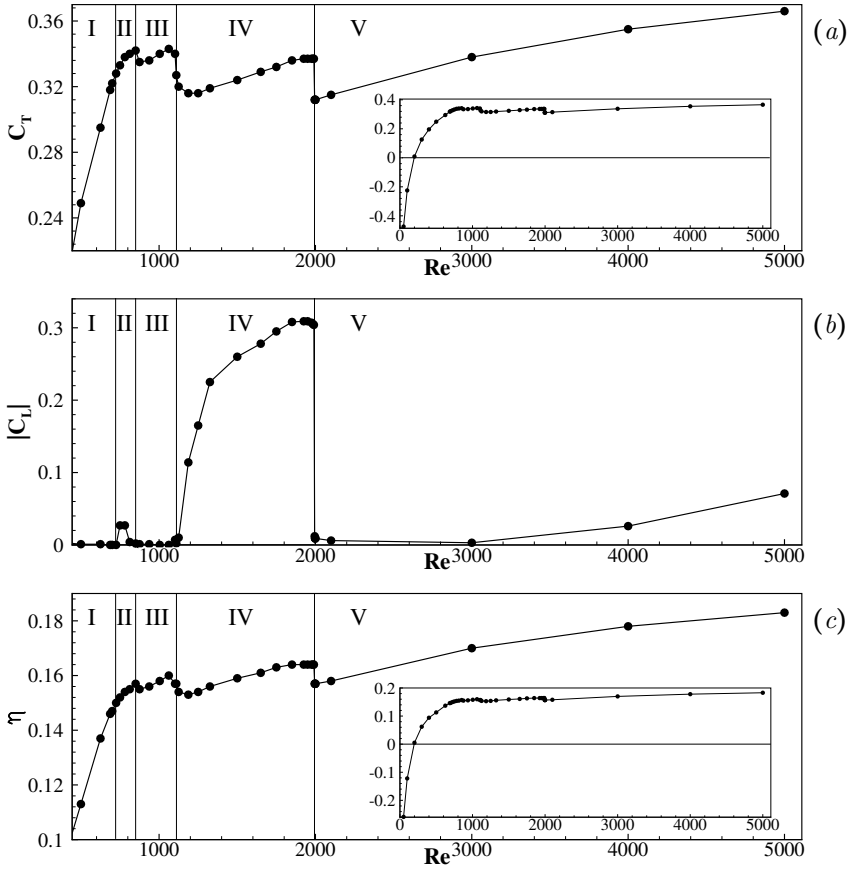

Figure 7: Behaviour of the thrust coefficient (a), lift coefficient (b) and of efficiency (c) as a function of Re for $(KC, kh) = (0.12, 0.9)$. The insets report the behaviours over all Reynolds numbers considered while the main panels show an enlargment of the behaviour for $Re > 450$.

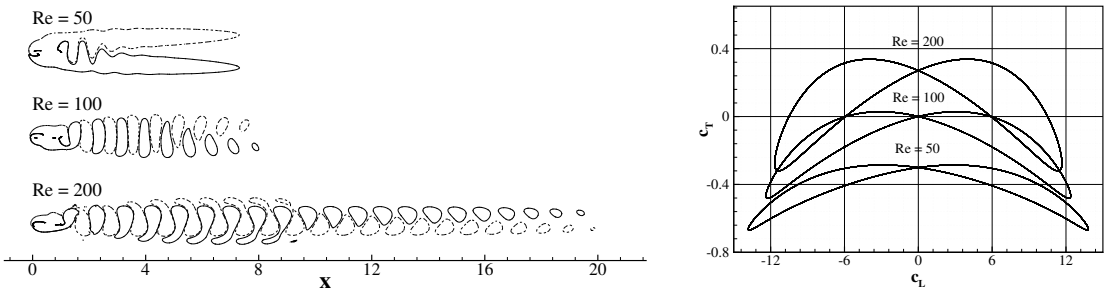

Figure 8: Instantaneous behaviour of the wake shown with isolines of $\omega_z = [-0.2, 0.2]$ for $(KC, kh) = (0.12, 0.9)$ as a function of the Reynolds number. Region I, $Re = 50, 100, 200$. The right panel reports the phase map (c_L, c_T) of the same flow cases.

Case	Re	C_T	C_L	C_P	η
C1	50	-0.474	null	-1.832	-0.259
C2	100	-0.225	null	-1.843	-0.122
C3	200	0.009	null	-1.963	0.005
C4	300	0.126	null	-2.032	0.062
C5	400	0.196	null	-2.078	0.094
C6	500	0.249	null	-2.121	0.113
C7	625	0.295	null	-2.151	0.137
C8	687	0.318	null	-2.182	0.146
C9	700	0.322	null	-2.187	0.147
C10	725	0.328	null	-2.191	0.150
C11	750	0.333	-0.027	-2.193	0.152
C12	781	0.338	-0.027	-2.194	0.154
C13	812	0.340	0.004	-2.186	0.155
C14	850	0.342	null	-2.186	0.157
C15	875	0.335	null	-2.167	0.155
C16	937	0.336	null	-2.158	0.156
C17	1004	0.340	null	-2.149	0.158
C18	1062	0.343	null	-2.141	0.160
C19	1102	0.340	null	-2.161	0.157
C20	1110	0.327	null	-2.089	0.157
C21	1125	0.320	0.010	-2.078	0.154
C22	1187	0.316	0.114	-2.061	0.153
C23	1250	0.316	0.165	-2.049	0.154
C24	1325	0.319	-0.225	-2.040	0.156
C25	1500	0.324	0.260	-2.045	0.159
C26	1650	0.329	0.278	-2.037	0.161
C27	1750	0.332	0.295	-2.040	0.163
C28	1850	0.336	0.308	-2.047	0.164
C29	1925	0.337	0.309	-2.052	0.164
C30	1950	0.337	0.309	-2.054	0.164
C31	1975	0.337	0.307	-2.056	0.164
C32	1985	0.337	0.305	-2.056	0.164
C33	1990	0.337	0.304	-2.056	0.164
C34	1995	0.312	0.012	-1.992	0.157
C35	1997	0.312	0.009	-1.994	0.157
C36	1999	0.312	0.009	-1.994	0.157
C37	2000	0.312	0.009	-1.994	0.157
C38	2100	0.315	0.006	-1.994	0.158
C39	3000	0.338	null	-1.993	0.170
C40	4000	0.355	0.026	-1.994	0.178
C41	5000	0.366	0.071	-1.997	0.183

Table 2: Parameters, aerodynamic coefficients and efficiency of the simulated flow cases for $(KC, kh) = (0.12, 0.9)$ and different Reynolds numbers.

The instantaneous flow topology of the wake and the phase diagrams (c_L, c_T) of the transition from drag to thrust conditions are reported in figure 8. For the lower Reynolds number cases characterized by the development of drag, $Re = 50$ and 100, the wake develops a classical von Kármán street which is rapidly dissipated. On the other hand, by passing the critical Reynolds number for $Re = 200$, the oscillating foil produces thrust and the wake is characterized by an inverted von Kármán street. The phase diagrams (c_L, c_T) clearly highlight the transition. The orbits follow a symmetric limit cycle ($C_L = 0$) for all the cases but by increasing the Reynolds number an upward shift is observed. In particular, for the lower Re case, the foil experiences drag for the entire oscillating period ($C_T < 0$) while, by increasing the Reynolds number, the upward shift of the orbits is such that for $Re = 200$ most of the time the foil experiences thrust leading to $C_T > 0$.

6.2. Region II

By entering region II, for $725 < Re < 850$, the increase of thrust and efficiency with the Reynolds number is less marked with respect to region I, see figure 7. This range of Reynolds numbers is characterized by the appearance of an interesting phenomenon whose signature is present in the behaviour of the lift coefficient. Indeed, by entering this region, C_L is found to increase reaching non-zero values of the order of $C_L \approx 0.03$ and to decrease going to zero again by leaving this region. The origin of such a phenomenon can be analysed by considering the instantaneous flow topology of the wake and the phase diagrams (c_L, c_T) reported in figure 9. Contrary to region I, an initially straight inverted von Kármán street is found to develop a deflection for $x > 8$ in region II. As shown by the phase diagram, this deflection of the wake is stationary being the orbits following an asymmetric limit cycle ($C_L \neq 0$).

6.3. Region III

As shown in figure 7, by entering region III for $850 < Re < 1110$, the lift coefficient is null and both the thrust and efficiency show a jump toward smaller values from $(C_T, \eta) = (0.342, 0.157)$ at $Re = 850$ to

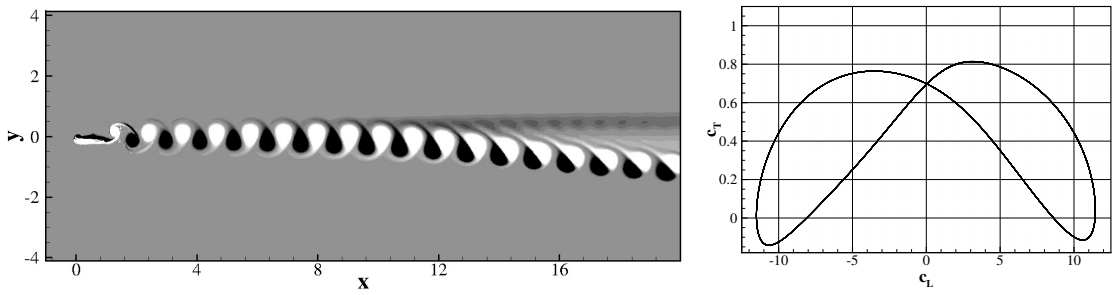

Figure 9: Instantaneous behaviour of the wake shown with isolines of $\omega_z = [-1, 1]$ for $(KC, kh) = (0.12, 0.9)$ as a function of the Reynolds number. Region II, $Re = 750$. The right panel reports the phase map (c_L, c_T) of the same flow case.

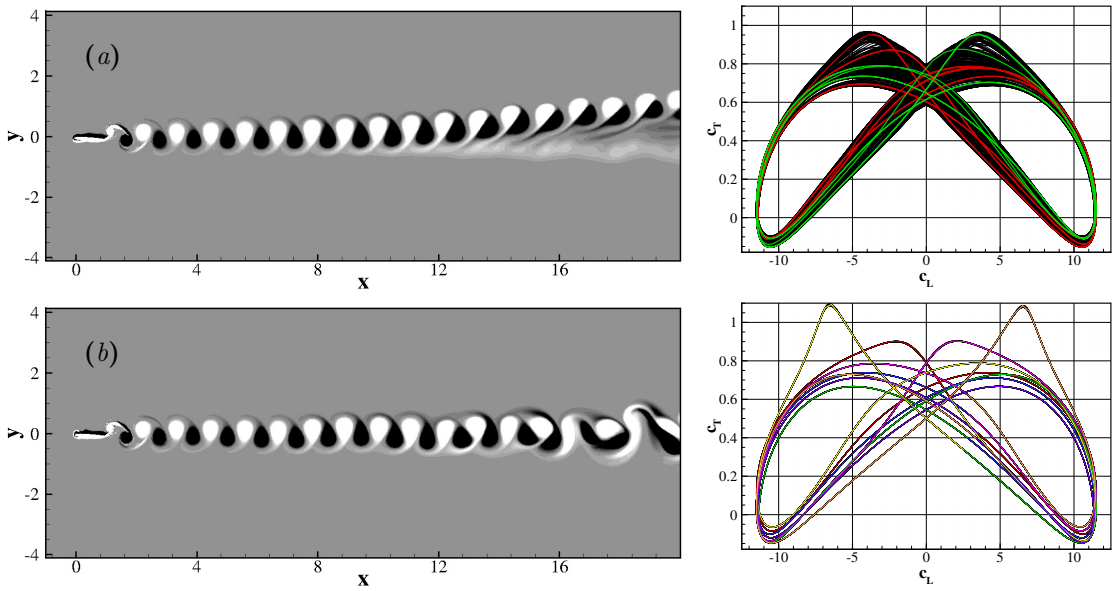

Figure 10: Instantaneous behaviour of the wake shown with isolines of $\omega_z = [-1, 1]$ for $(KC, kh) = (0.12, 0.9)$ as a function of the Reynolds number. Region III, $Re = 875$ (a) and $Re = 937$ (b). The right panels report the phase map (c_L, c_T) of the corresponding flow cases.

$(C_T, \eta) = (0.335, 0.155)$ at $Re = 875$ before attaining again an increasing behaviour with Re. The discontinuity in the aerodynamic performances at the beginning of this region, is associated with the appearance of different unsteadiness phenomena. Indeed, in the very first part of region III, for $850 < Re < 875$, the zero value of the lift coefficient is not attained by the recovery of a simple straight wake as it is for region I. Indeed, as shown in figure 10(a), the wake is found to be still characterized by a deflected inverted von Kármán street as it is for the non-zero average lift occurring at lower Reynolds numbers in region II. However, the deflection is now not stationary so that the occurrence of periodic inversions of the deflection of the wake leads on average to a zero lift. This phenomenon can clearly appreciated by considering the phase diagram shown again in figure 10(a). Indeed, the orbits are found to lie in a region in the space of phases forming a symmetric strange attractor. A careful inspection of the paths, green and red lines in the phase diagram of panel 10(a), reveals that the orbits follow an asymmetric strange attractor (locked deflected wake) for relatively long times of the order of $\mathcal{O}(80)$ oscillating periods before switching to the opposite asymmetric attractor (inversion of the deflection of the wake) thus recovering on average a symmetric attractor ($C_L = 0$).

In the second part of region III, for $875 < Re < 1004$, a second instability mode appears. As shown in panel 10(b), the wake recovers a straight behaviour leading as a consequence to a null lift coefficient.

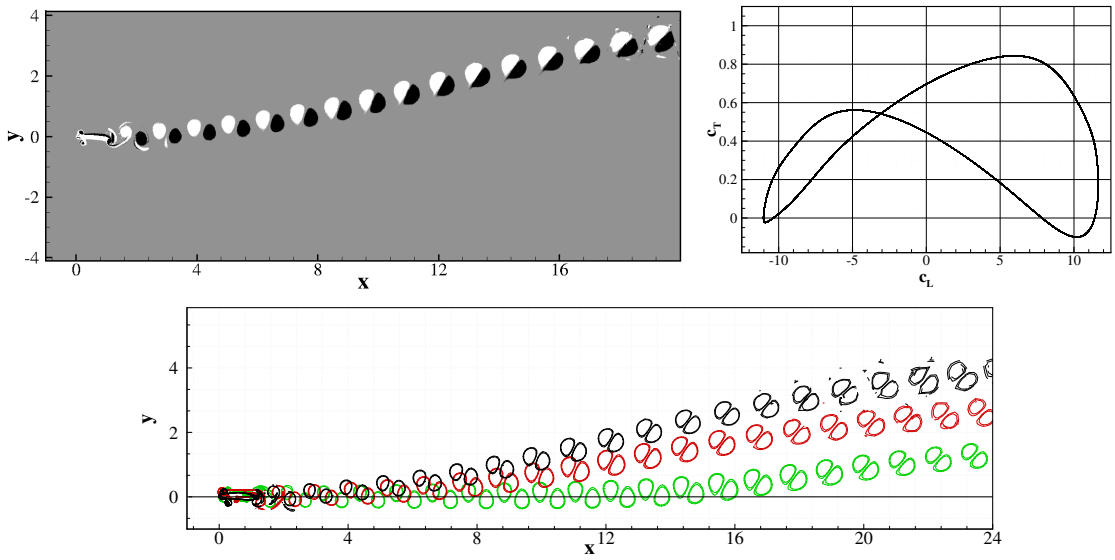

Figure 11: Instantaneous behaviour of the wake shown with isolines of $\omega_z = [-1, 1]$ for $(KC, kh) = (0.12, 0.9)$ as a function of the Reynolds number. Region IV, $Re = 1850$. The right panel reports the phase map (c_L, c_T) of the same flow case. In the bottom plot, the behaviour of the wake for $Re = 1125$ (green), $Re = 1187$ (red) and $Re = 1850$ (black) is shown with isolines of $\omega_z = [-3, 3]$.

However, in this case, an unstable mode appears in the wake for $x > 11$. The strength of this phenomenon is such that the coherent pattern of the wake is not completely destroyed and, as a consequence, the wake region remains confined in a relatively thin layer. Interestingly, despite the apparent complex chaotic feature of the wake for $x > 11$, as shown by the phase diagram in panel 10(b), the associated instability follows a well coherent pattern. Indeed, the orbits in the space of phases trace a well-defined limit cycle. As shown by the different coloured lines corresponding each to a single oscillating period, the emerging limit cycle is found to be composed by 7 oscillating periods which are exactly repeated over the entire simulation time without any appearance of deviation from it.

Region III is finally closed by a third instability mode, for $1004 < Re < 1110$, which resembles the one occurring in the first part of the region, i.e. an unsteady deflected wake experiencing inversion whose phase diagram is a strange symmetric attractor ($C_L = 0$). The only difference comes from the fact that the period of inversion of deflection of the wake is significantly reduced with respect to that observed in the very first part of region III, being now of the order of $\mathcal{O}(45)$ oscillating periods. Being the differences between these two parts of region III of solely quantitative nature, the wake pattern and phase diagrams are not shown for brevity reasons.

6.4. Region IV

By entering region IV, corresponding to the range $1110 < Re \leq 1990$, both thrust and efficiency show a sharp decrease, see figure 7, before attaining again an increase of their values with the Reynolds number. In this region, the most evident effect of the Reynolds number takes the form of a significant increase of lift with Re. As already shown in section 5, these values of non-zero lift are associated with the appearance of an asymmetric phenomenon of stable deflection of the wake, see the wake pattern and the phase diagram reported also in the top panels of figure 11.

The origin of the increase of lift with the Reynolds number is shown in the bottom panel of figure 11. As it can be seen, for $Re = 1125$ the wake shows a late deflection for $x > 14$ while for $Re = 1187$ the deflection of the wake occurs for $x > 4$. Hence, we argue that the initial growth of the lift coefficient is given by the upstream rising of the wake deflection. This behaviour is attained up to $Re = 1250$ where the deflection of the wake takes place immediately behind the foil. Indeed, for $1250 < Re \leq 1990$, the increase of the

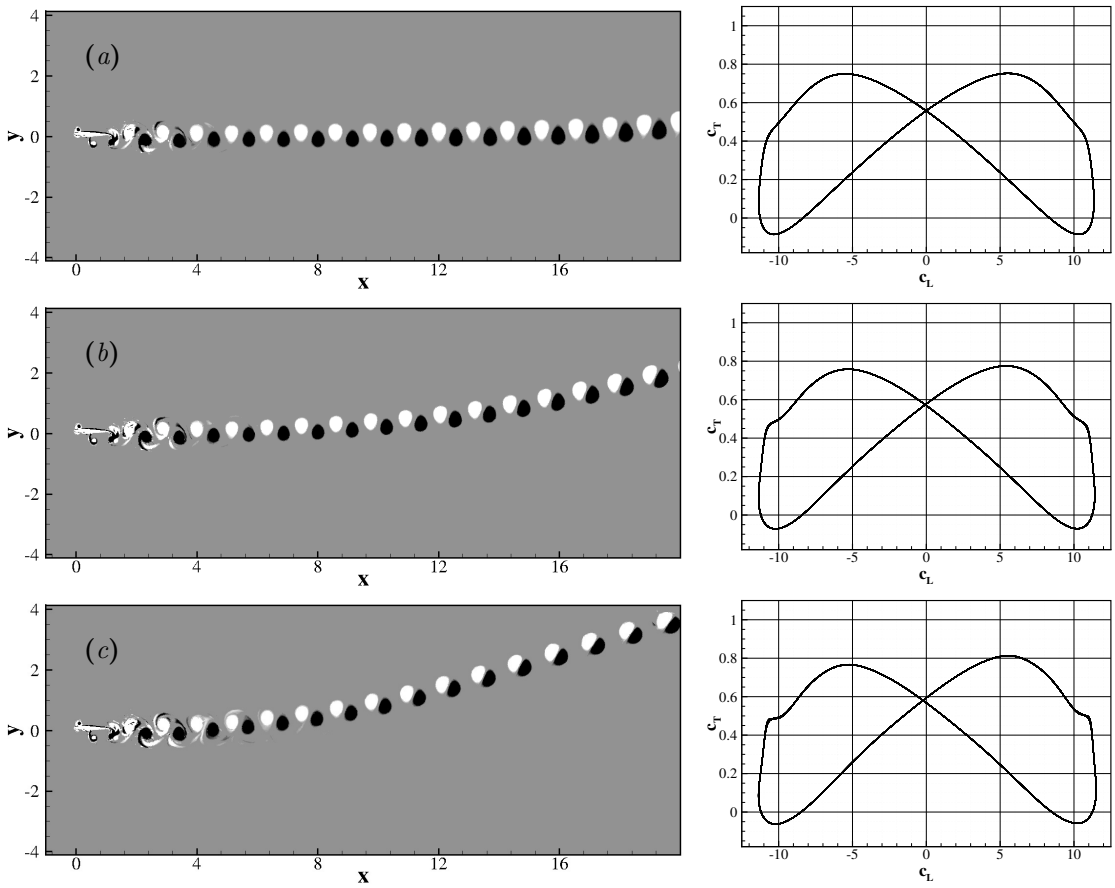

Figure 12: Instantaneous behaviour of the wake shown with isolines of $\omega_z = [-1, 1]$ for $(KC, kh) = (0.12, 0.9)$ as a function of the Reynolds number. Region V, $Re = 3000$ (a), $Re = 4000$ (b) and $Re = 5000$ (c). The right panel reports the phase map (c_L, c_T) of the corresponding flow cases.

lift coefficient is ascribed to an increase of the inclination of the deflection. Accordingly, in the bottom panel of figure 11, it can be seen an increase of the inclination of the wake from $Re = 1187$ to $Re = 1850$. Interestingly, this behaviour of lift and also of thrust and efficiency abruptly changes by entering region V for $Re > 1990$.

6.5. Region V

As already mentioned, by crossing the critical Reynolds number $Re = 1990$, the thrust, efficiency and lift coefficients experience a sharp transition to the last regime investigated in this work. As shown in figure 7, both thrust and efficiency show a step behaviour from $C_T = 0.337$ and $\eta = 0.164$ at $Re = 1990$ to lower values $C_T = 0.312$ and $\eta = 0.157$ at $Re = 1995$. After this sharp transition, an increase of both thrust and efficiency is found to take place again reaching their highest values, i.e. $C_T = 0.366$ and $\eta = 0.183$. On the other hand, also the lift coefficient experiences a step behaviour from $C_L = 0.304$ at $Re = 1990$ to $C_L = 0.012$ at $Re = 1995$. After this sharp transition, the lift coefficient approaches first a weak decrease behaviour towards the zero value up to $Re = 3000$ and then increases again showing non zero values.

As shown in panel 12(a), the first part of this final regime is characterized by an almost straight inverted von Kármán street that in the space of phases follows a symmetric limit cycle analogously to the behaviour observed in region I. The only difference with region I is of quantitative nature being now the values of thrust and efficiency larger, see figure 7 and the upward shift of the phase diagram of panel 12(a) with respect to that of panel 8. For $Re > 3000$, the lift coefficient starts to increase and, as shown in figure 12(b)

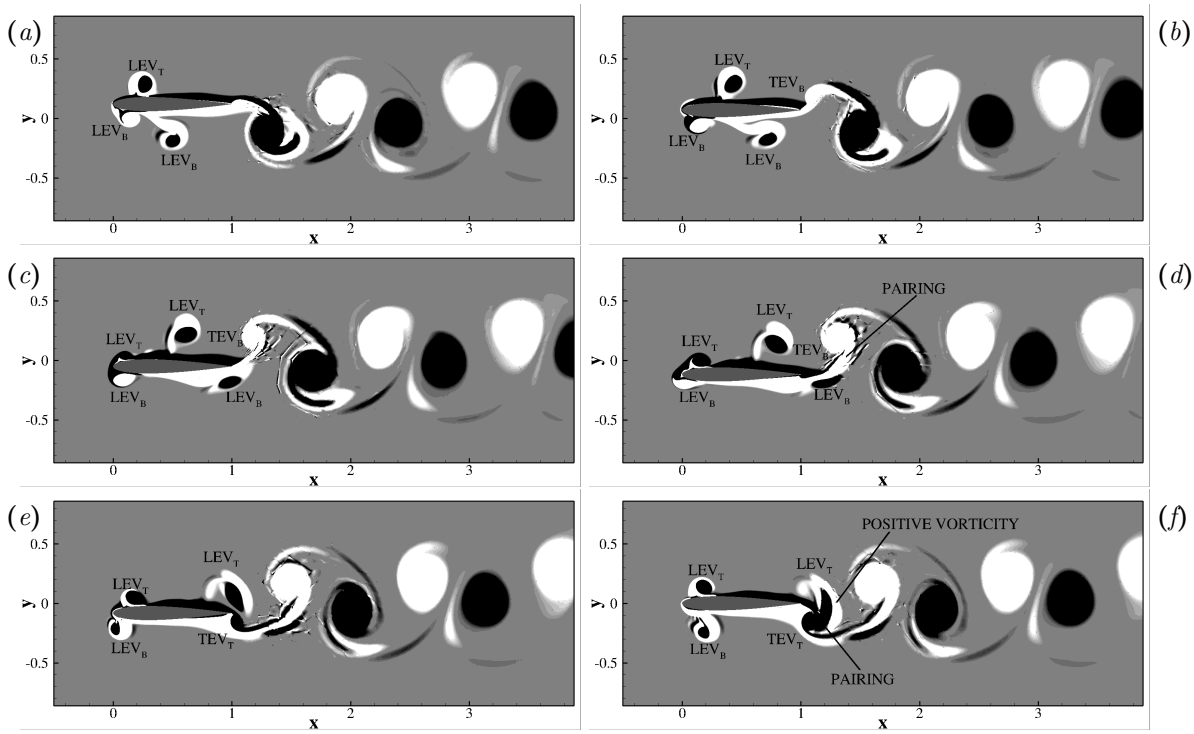

Figure 13: Instantaneous behaviour of the shedding of vortices shown with isocontours of $\omega_z = [-1, 1]$ for $(KC, kh) = (0.12, 0.9)$ and $Re = 1990$. Six equally spaced instants covering an oscillating period are shown from panel (a) to (f), respectively.

and (c), a stable deflection of the wake occurs. Similarly to region IV, by increasing the Reynolds number, an upstream rising of the deflection and an increase of the inclination is observed. As shown by the phase diagrams in figure 12(b) and (c), the main difference with respect to region IV is that the asymmetry of the limit cycle is less pronounced, in accordance with the lower values of lift reproduced at these Reynolds numbers. This weak asymmetry of the limit cycle is recognized to be at the basis of the large values of thrust measured in this region. Indeed, despite the fact that the highest values of thrust reproduced during each oscillating periods are less intense with respect to those reached in region IV, compare the phase diagrams of figures 12(b) and (c) with that of figure 11, the more symmetric behaviour of the orbits is such that the foil express high levels of thrust for a larger fraction of the oscillating period thus leading to higher values of thrust on average.

7. A note on the leading-edge vortex shedding and the Reynolds-dependent flow transition

It is well known that the wake pattern is essentially determined by the fate of the leading-edge vortices (LEV), whether or not are shed, and their interactions with the trailing-edge vortices (TEV) (Lewin and Haj-Hariri, 2003). For this reason, in this section we report a note on their role in the Reynolds-dependent transitions shown in the previous section. In particular, we consider the sharp flow transition splitting the flow regimes of region IV and V that occurs by increasing the Reynolds number from $Re = 1990$ to $Re = 1995$. Let us recall that this transition consists in a sudden recovery of a straight inverted von Kármán street from a stable deflected one.

We start by considering the behaviour of the leading- and trailing-edge vortices and their interactions for the flow case at $Re = 1990$. As shown in figure 13(a), vortices are found to detach from the leading edge during both the up and down stroke. More importantly, figure 13(a) also unveils that the origin of the flow symmetry breaking, typical of the flow cases with deflected wakes, can be traced back to the flow pattern induced by the top and bottom leading-edge vortices, LEV_T and LEV_B respectively. Indeed, both LEV_T

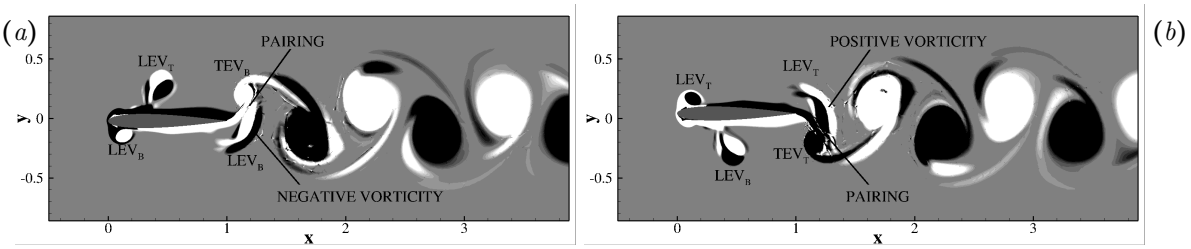

Figure 14: Instantaneous behaviour of the shedding of vortices shown with isocontours of $\omega_z = [-1, 1]$ for $(KC, kh) = (0.12, 0.9)$ and $Re = 1995$. Two equally space instants covering an oscillating period are shown in panel (a) and (b).

and LEV$_B$ consist of two counter-rotating vortices embedded each other without a symmetry reflection of the sign of rotation in the top and bottom sides of the foil. The inner vortex has a negative vorticity and the outer one has a positive vorticity both for LEV$_T$ and LEV$_B$. This fail of reflection symmetry can be ascribed to the timing of detachment of vortices in the top and bottom sides of the foil as detailed below.

Let us consider the behaviour of the bottom side of the foil. The leading-edge separation bubble at the bottom of the foil is generated after half of each upstroke period (see the upstream LEV$_B$ in panel 13(a)) and remains attached to the body for the rest of it and for the successive downstroke (see the upstream LEV$_B$ in panels 13(b), (c) and (d)) eventually being shed with a finite phase shift $0.17/f$ after the end of the downstroke (see the upstream LEV$_B$ in panels 13(e) and (f)). In particular, the separation bubble is not able to follow the downward kinematic of the foil during the downstroke and it moves upstream and upward thus interacting with the motion of the recirculating bubble in the top of the foil (see the upstream LEV$_B$ in panels 13(b), (c) and (d)). This upward and upstream movement of the bubble is at the basis of the formation of a vortex with negative vorticity embedded in positive vorticity. Indeed, during the generation of the separation bubble (see the upstream LEV$_B$ in panels 13(a), (b) and (c)), the negative vorticity starts to surround the bubble as it commonly happen in separated flows, but the upstream and upward advection of the separation bubble in the final period of the downstroke leads to a deformation of the bubble itself so that eventually positive vorticity surrounds a negative vorticity core (see the upstream LEV$_B$ in panels 13(d) and (e)). A different scenario is observed in the top side of the foil. The separation bubble in the top of the foil is generated after half of each downstroke period (see the upstream LEV$_T$ in panel 13(c)), exactly as in the bottom side. However, as opposed to the bottom side, the separation bubble in the top side remains attached to the foil without moving upstream for the rest of the downstroke period and for the successive upstroke period (see the upstream LEV$_T$ in panel 13(d), (e) and (f)) eventually being shed exactly at the end of the upstroke without phase shift (see the upstream LEV$_T$ in panel 13(a) and (b)).

The fail of symmetry reflection in the formation of the leading-edge vortices and the asymmetric time of their shedding (exactly at the end of the upstroke for LEV$_T$ and after the end of the downstroke with a finite phase delay $0.17/f$ for LEV$_B$) are at the basis of the symmetry breaking of the wake pattern. Indeed, as shown in panels 13(e) and (f) the leading-edge vortex from the top side LEV$_T$ interacts with the trailing-edge vortex TEV$_T$ immediately after its shedding. On the other hand, the leading-edge vortex from the bottom side LEV$_B$ lately interacts with the trailing-edge vortex TEV$_B$, see panels 13(c) and (d) where the pairing of the two vortices is shown to occur at locations further downstream with respect to those of the pairing of LEV$_T$ with TEV$_T$ shown in panels 13(e) and (f). All these aspects give rise to an inverted von Kármán street that, during the downstroke is characterized by a couple of counter-rotating vortices inducing a flow motion pointing in the upward direction, see panel 13(d). On the other hand, the inverted von Kármán street during the upstroke is characterized by a region of positive vorticity within two counter-rotating vortices whose action is to dump the induced flow motion pointing in the downward direction, see panel 13(f). This asymmetry in the flow motion induced by the counter-rotating pairs of vortices is at the basis of the stable deflection of the inverted von Kármán street observed at $Re = 1990$.

By slightly increasing the Reynolds number to $Re = 1995$, both the fail of symmetry reflection in the formation of the leading-edge vortices and the phase shift in the shedding of the leading-edge vortices from the top and bottom side of the foil disappear, see figure 14. Indeed, the leading-edge vortices are found to

be constituted by a triple structure of alternated sign of vorticity with symmetry reflection in the two sides of the foil that are detached at the end of the each downstroke/upstroke without phase shift. As a result, the leading-edge vortices from both the two sides, LEV_T and LEV_B, are found to equally interact with the respective trailing-edge vortices, TEV_T and TEV_B, thus leading to a straight inverted von Kármán street, see panels 14(a) and (b).

This analysis confirms that the asymmetric timing of shedding of the leading-edge vortices is crucial for the generation of a deflected inverted von Kármán street and, hence, for the related aerodynamic performances. In this context, we found that the Reynolds number is a fundamental parameter for these symmetry breaking phenomenon.

8. Conclusions

The formation of fascinating fluid flow phenomena and the generation of aerodynamic forces of great significance for a plethora of applications, are at the basis of the scientific interest on the paradigmatic flow around oscillating foils. However, after decades of research efforts the problem is still recognized as extremely elusive. The reason is the complex kinematics and dynamics of the flow. Furthermore, the dependency of the flow on multiple parameters characterizing the foil oscillation, challenge for a rational approach. Indeed, the flow can be described from a kinematic point of view as a function of the ratio between the heave and free-stream velocity kh and as a function of the ratio between the heave amplitude and the chord of the foil KC. On the other hand, from a dynamic point of view, the flow can be described as a function of the ratio between inertial and viscous forces, the Reynolds number Re. Most of literature results concentrate their efforts to the study of the flow properties as a function of the couple of parameters (kh, KC) while less attention has been devoted to the role of the Reynolds number. Here, in order to address the individual role of each parameter governing the flow performance, we performed high-order accurate numerical simulations which clearly identify variations in the three-dimensional space of parameters (kh, KC, Re). The aim is to explore how the Reynolds number influence basic aspects of the flow such as the structure of the wake and the associated aerodynamic forces at different values of the kinematic parameters (kh, KC). Very interesting phenomena and behaviours appear with a clearly identified origin in the parameter space thus proving the importance of using a rational approach such as that used in the present work.

We found that the Reynolds number is responsible for significant variations of the aerodynamic forces exerted by the oscillating foil. In analogy with the heave velocity ratio kh that has been widely used to identify the critical conditions for the development of thrust, it is shown that also the Reynolds number plays this role by defining critical values above which thrust conditions are developed. Furthermore, the Reynolds number is found to be also at the basis of different transitional phenomena leading to the appearance of flow instabilities such as stable and quasi-periodically switching deflected wakes. As an example, for a fixed value of heave velocity and amplitude, $(kh, KC) = (0.9, 0.12)$, we found the presence of a critical Reynolds number, $Re_c = 200$, such that the oscillating foil experiences drag for $Re < Re_c$ while a recovery of thrust conditions is obtained for $Re > Re_c$. On the other hand for the same flow case , $(kh, KC) = (0.9, 0.12)$, we found that by varying the Reynolds number for $Re > Re_c$, the structure of the flow and the aerodynamic forces experience also different smooth and sharp transitions. Among many others interesting phenomena, it is found that by increasing the Reynolds number, the structure of the flow moves from a straight inverted von Kármán street to a stable deflected one before sharply recovering again a straight inverted von Kármán street. Hence, subcritical values of the Reynolds number for smooth and sharp transitions of the flow structure and performance are also identified.

In this context, the space of phases (c_L, c_T) is recognized to be fundamental for the understanding of the physical evolution of the system and of the cyclical phenomena composing it. Indeed, we have shown how the analysis of the orbits in the space of phases allows us to understand how the thrust and lift forces are developed during the oscillating period and how the presence of low frequency unsteadinesses recursively modify this scenario. It is finally worth pointing out that the identified instabilities are very low-frequency phenomena. As an example the period of switching of the deflection of the wake is found to be two orders of magnitude greater than the heave period. The presence of these very slow unsteadinesses challenges for numerical simulations and the use of the phase diagrams could help to clarify also this issue. Indeed, the

analysis of the orbits in the space of phases during simulation is also found to be a very useful technique for the identification of the presence of very slow transitional phenomena transporting the flow from one state to another one.

Appendix A. On the triads of governing parameters

In section 2, we have introduced the three governing parameters,

$$St = \frac{fc}{U_\infty} \; ; \qquad KC = \frac{h}{c} \; ; \qquad Re = \frac{U_\infty c}{\nu} \; ; \tag{A.1}$$

which are connected with the following non-dimensionalization of the aerodynamic forces

$$C_D = \frac{D}{1/2\rho s c U_\infty^2} \qquad C_L = \frac{L}{1/2\rho s c U_\infty^2} \tag{A.2}$$

In the procedure, ρ has been used to drop the dimension of mass, $\sqrt{sc}$ to drop the dimension of length and, finally, c/U_∞ to drop the dimension of time. This is the classical procedure commonly adopted for the study of aerodynamics bodies. However, this approach does not make use of all the dimensional arguments related with the flow oscillation. Indeed, by using quantities that are solely related to the phenomenon of oscillation, other non-dimensional groups can be obtained. Indeed, by using ρ to drop the dimension of mass, $\sqrt{ch}$ to drop the dimension of length and finally $1/f$ to drop the dimension of time, one recovers the following dimensionless groups,

$$C'_D = \frac{D}{1/2\rho V^2 c^2} = f\left(\frac{V}{U_\infty}, \frac{h}{c}, \frac{Vc}{\nu}\right) \qquad C'_L = \frac{L}{1/2\rho V^2 c^2} = g\left(\frac{V}{U_\infty}, \frac{h}{c}, \frac{Vc}{\nu}\right) \tag{A.3}$$

where, the governing parameters in this case are,

$$kh = \frac{V}{U_\infty} = 2\pi KC \; St \; ; \qquad KC = \frac{h}{c} \; ; \qquad \beta = \frac{Vc}{\nu} = kh \; Re = 2\pi KC \; St \; Re \; ; \tag{A.4}$$

where we recognize that only the physical meaning of the heave amplitude parameter KC remains unaltered with respect to the groups used in the present work. Indeed, kh is not any more the Strouhal number of the oscillation but the heave velocity amplitude, $kh = V/U_\infty$. The link between these two parameters is given by the heave amplitude as $kh = 2\pi KCSt$. Finally, the parameter β represents a Reynolds number but it is not connected any more with the free-stream conditions but with the velocity of the oscillation, $\beta = Vc/\nu$. The two definitions of Reynolds number are connected each other by the kinematics parameters of the oscillation (heave frequency and amplitude) as, $\beta = 2\pi KCStRe$. These governing parameters are related with a non-dimensionalization of the aerodynamic performances (A.3) which is different with the classical one (A.2) commonly used in non-oscillating foils. The two definitions of aerodynamic coefficients are related each others by the following relations

$$C'_{D,L} = \frac{C_{D,L}}{kh^2} = \frac{C_{D,L}}{(2\pi KC \; St)^2} \tag{A.5}$$

thus unveiling that the quadratic behaviour of the classical aerodynamic coefficients with the frequency of the oscillation (Garrick, 1936; Triantafyllou et al., 1991; Lai and Platzer, 1999; Floryan et al., 2017) is naturally absorbed in the definition itself of the new aerodynamic coefficients (A.3). It is worth reminding that this difference is simply due to the fact that in the alternative dimensional analysis we used only dimensional arguments related with the flow oscillation. As a consequence, the obtained governing parameters (kh, KC, β) result to be strictly related to the main features of the foil oscillation and retain a well-defined physical interpretation while the aerodynamic coefficients are found to absorb relevant scaling. Establishing whether the alternative dimensional groups (A.3) allow for a detection of relevant asymptotic behaviours of oscillating foils would require the use of additional simulations and exceeds the scope of the present work and, hence, is postponed to future dedicated works.

References

R. Knoller, Die gesetze des luftwiderstandes, Flug und Motortechnik (Wien) 3 (1909) 1–7.

A. Betz, Ein beitrag zur erklärung des segelfluges, Zeitschrift für Flugtechnik und Motorluftschiffahrt 3 (1912) 269–272.

T. von Kármán, General aerodynamic theory-perfect fluids, Aerodynamic theory 2 (1935) 346–349.

R. Godoy-Diana, J.-L. Aider, J. Wesfreid, Transitions in the wake of a flapping foil, Phys. Rev. E 77 (2008) 016308.

R. Godoy-Diana, C. Marais, J.-L. Aider, J. Wesfreid, A model for the symmetry breaking of the reverse Bénard-von Kármán vortex street produced by a flapping foil, J. Fluid Mech. 622 (2009) 23–32.

A. Das, R. Shukla, R. Govardhan, Existence of a sharp transition in the peak propulsive efficiency of a low-Re pitching foil, J. Fluid Mech. 800 (2016) 307–326.

Z. Zheng, Z. Wei, Study of mechanisms and factors that influence the formation of vortical wake of a heaving airfoil, Phys. Fluids 24 (2012) 103601.

Z. Wei, Z. Zheng, Mechanisms of wake deflection angle change behind a heaving airfoil, J. Fluids Struct. 48 (2014) 1–13.

I. E. Garrick, Propulsion of a flapping and oscillating airfoil, Technical Report, NACA Tech. Rep. 567, 1936.

T. Theodorsen, General theory of aerodynamic instability and the mechanism of flutter, NACA Thecnical Report (1935).

M. Triantafyllou, G. Triantafyllou, R. Gopalkrishnan, Wake mechanics for thrust generation in oscillating foils, Phys. Fluids A 3 (1991) 2835–2837.

J. Lai, M. Platzer, Jet characteristics of a plunging airfoil, AIAA journal 37 (1999) 1529–1537.

D. Floryan, T. Van Buren, C. Rowley, A. Smits, Scaling the propulsive performance of heaving and pitching foils, J. Fluid Mech. 822 (2017) 386–397.

K. Jones, C. Dohring, M. Platzer, Experimental and computational investigation of the knoller-betz effect, AIAA journal 36 (1998) 1240–1246.

G. Lewin, H. Haj-Hariri, Modelling thrust generation of a two-dimensional heaving airfoil in a viscous flow, J. Fluid Mech. 492 (2003) 339–362.

A. Andersen, T. Bohr, T. Schnipper, J. Walther, Wake structure and thrust generation of a flapping foil in two-dimensional flow, J. Fluid Mech. 812 (2017).

M. Visbal, High-fidelity simulation of transitional flows past a plunging airfoil, AIAA journal 47 (2009) 2685–2697.

U. Senturk, A. Smits, Reynolds number scaling of the propulsive performance of a pitching airfoil, AIAA Journal (2019) 2663–2669.

T. Van Buren, D. Floryan, N. Wei, A. Smits, Flow speed has little impact on propulsive characteristics of oscillating foils, Phys. Rev. Fluids 3 (2018) 013103.

K. Isogai, Y. Shinmoto, Y. Watanabe, Effects of dynamic stall on propulsive efficiency and thrust of flapping airfoil, AIAA journal 37 (1999) 1145–1151.

M. Ashraf, J. Young, J. Lai, Reynolds number, thickness and camber effects on flapping airfoil propulsion, J. Fluids Struct. 27 (2011) 145–160.

M. Dave, A. Spaulding, J. Franck, Variable thrust and high efficiency propulsion with oscillating foils at high Reynolds numbers, Ocean Engineering 214 (2020) 107833.

F. Bassi, A. Crivellini, S. Rebay, M. Savini, Discontinuous Galerkin solution of the Reynolds averaged Navier-Stokes and k - ω turbulence model equations, Computers & Fluids (2005) 507–540.

F. Bassi, A. Crivellini, D. Di Pietro, S. Rebay, An implicit high-order discontinuous Galerkin method for steady and unsteady incompressible flows, Computers & Fluids 36 (2007) 1529–1546.

A. Crivellini, V. D'Alessandro, F. Bassi, A Spalart-Allmaras turbulence model implementation in a discontinuous Galerkin solver for incompressible flows, Journal of Computational Physics 241 (2013a) 388 – 415.

A. Crivellini, V. D'Alessandro, F. Bassi, High-order discontinuous Galerkin solutions of three-dimensional incompressible RANS equations, Computers & Fluids 81 (2013b) 122 – 133.

F. Bassi, A. Crivellini, D. A. Di Pietro, S. Rebay, An artificial compressibility flux for the discontinuous Galerkin solution of the incompressible Navier-Stokes equations, Journal of Computational Physics 218 (2006) 794–815.

J. Lang, J. Verwer, ROS3P—An accurate third-order Rosenbrock solver designed for parabolic problems, BIT 41 (2001) 731–738.

M. Franciolini, L. Botti, A. Colombo, A. Crivellini, p-Multigrid matrix-free discontinuous Galerkin solution strategies for the under-resolved simulation of incompressible turbulent flows, Computers & Fluids 206 (2020) 104558.

E. Guilmineau, P. Queutey, A numerical simulation of vortex shedding from an oscillating circular cylinder, Journal of Fluids and Structures 16 (2002) 773 – 794.

W. Gu, C. Chyu, D. Rockwell, Timing of vortex formation from an oscillating cylinder, Physics of Fluids 6 (1994) 3677–3682.

C. Bose, S. Sarkar, Investigating chaotic wake dynamics past a flapping airfoil and the role of vortex interactions behind the chaotic transition, Phys. Fluids 30 (2018) 047101.

C. Williamson, A. Roshko, Vortex formation in the wake of an oscillating cylinder, Journal of fluids and structures 2 (1988) 355–381.

S. Heathcote, I. Gursul, Jet switching phenomenon for a periodically plunging airfoil, Phys. Fluids 19 (2007) 027104.